RSC Advances

PAPER

View Article Online
View Journal | View Issue

Cite this: *RSC Adv.*, 2025, **15**, 25885

Synthesis, characterization, and photophysical properties of europium complex-functionalized fumed silica and its corresponding PMMA-doped composites†

Qiuping Li, *[a] Hongxia Ouyang,[a] Xinghui Yang,[a] Qi Wang,[a] Yonghong Ding,[a] Haichao Yu[a] and Zhi Rao[b]

Received 14th May 2025
Accepted 16th July 2025

DOI: 10.1039/d5ra03377b

rsc.li/rsc-advances

Lanthanide organic–inorganic hybrid fluorescent materials are considered as promising candidates for next-generation lighting materials due to their unique optical properties and potential applications. In this work, commercialized silica materials (fumed silica) were selected as the carrier. By means of the bridging function of silane coupling agents, $Eu(TTA)_3(Phen)$ was covalently grafted onto the surface of fumed silica to synthesize lanthanide hybrid phosphors. Subsequently, the phosphor was dispersed into the MMA polymerization system, and a monolithic fluorescent organic glass was fabricated *via in situ* polymerization. Both the obtained europium hybrid phosphor and the europium complex-doped organic glass exhibited intense red fluorescence under UV light and possessed the characteristics of broad absorption, narrow emission, and long fluorescence lifetime. The design and synthesis process is straightforward and cost-effective, making this approach highly valuable for the development and advancement of novel rare earth hybrid luminescent materials.

1. Introduction

Due to their unique electronic structures, lanthanide elements play a crucial role in various fields such as optical materials,[1–5] catalytic materials,[6–8] hydrogen storage materials[9–11] and magnetic materials.[12–15] Because of the energy-level crossing, when lanthanide elements lose their outer electrons and form ions, their 4f electron shell remains shielded by the fully occupied $5s^2$ $5p^6$ orbitals. Consequently, the influence of the crystal field environment on these orbitals is minimal. Thus, the extremely small energy level differences within the 4f orbitals result in narrow-band emission in their fluorescence behavior.[16–21] This is also the primary reason that lanthanide luminescent materials typically exhibit high fluorescence color purity and vivid hues. In addition, lanthanide luminescent materials exhibit high quantum efficiency, broad spectral coverage, and a wide range of fluorescence lifetimes. As a result, they are widely used in areas such as lighting,[22–25] sensing,[26–29] biological imaging,[30–32] and anti-counterfeiting.[33–35] Notably, inorganic rare earth luminescent materials dominate in the lighting area.[36–38] For a long time, significant efforts have been dedicated to the synthesis and investigation of inorganic rare earth luminescent materials. The primary objective is to enhance their quantum efficiency, thereby reducing the consumption of rare earth elements.

Since the rare earth is non-renewable resources and their extraction and purification demand substantial financial and material investments, researchers have been actively exploring various technologies that can achieve high-efficiency luminescence with reduced reliance on rare earth elements. Lots of studies have demonstrated that coordinating lanthanide ions with organic ligands, such as carboxylic acids,[39–42] β-diketones,[43–47] and so on can significantly enhance their photoluminescence efficiency. This is because these organic ligands exhibit high absorption coefficients in the ultraviolet region. Upon forming complexes with lanthanide ions, these ligands can transfer energy to the lanthanide ions *via* the "antenna effect," thereby sensitizing their luminescence.[48–52] However, pure lanthanide complexes exhibit limitations such as poor photo-stability, thermal stability, and processability, which have significantly hindered their practical applications. To address these issues, researchers have explored incorporating lanthanide complexes into specific matrix materials, aiming to compensate for the deficiencies of lanthanide luminescent materials through hybridization.[53–57] Furthermore, hybridization not only reduces the consumption of rare earth elements but also mitigates the concentration quenching effect in lanthanide luminescent materials, thereby playing a crucial role

[a]*FuZhou AI Drug Innovation Center, School of Pharmacy, Fuzhou Medical College of Nanchang University, Fuzhou 344000, China. E-mail: liqiuping@yeah.net*

[b]*Applied System Engineer, Gandong University, Fuzhou, Jiangxi 344000, China*

† Electronic supplementary information (ESI) available. See DOI: https://doi.org/10.1039/d5ra03377b

in the efficient utilization of rare earth resources. Thus, numerous work have been carried out to develop the lanthanide hybrid luminescent materials.[58–60] The lanthanide complexes have been continuously incorporated into various matrices, including silica,[61–63] zeolite,[64–66] clay,[67–69] polymers,[70–72] *etc.* Over the past decades, researchers from all over the world have proposed a multitude of synthetic strategies for lanthanide hybrid luminescent materials and fabricated numerous types of such materials with superior performance.[73]

Among the various matrices utilized for the preparation of lanthanide hybrid luminescent materials, silica materials are undoubtedly the most commonly selected. This is not only due to their low cost and ease of availability, as well as their excellent stability, but also because they can be engineered into diverse morphologies, such as spherical, porous, and gel-like structures.[74–79] Additionally, the surface properties of silica materials are relatively reactive, rendering them highly amenable to modification and composite formation. Although numerous silicon-based lanthanide hybrid materials have been synthesized over the past few decades, the majority of research efforts remain at the experimental stage. To achieve large-scale commercialization, several key challenges must be addressed, including reducing material production costs, simplifying synthesis procedures, *etc.* Therefore, to further demonstrate the feasibility of developing lanthanide composite luminescent materials based on silica, this work employed fumed silica, which is already well-established in commercial applications, as the carrier. Through molecular bridging, the lanthanide complex $Eu(TTA)_3(Phen)$, known for its excellent fluorescence emission properties, was successfully loaded onto fumed silica. Subsequently, it was incorporated into the PMMA matrix to fabricate a fluorescent organic glass with superior luminescent performance.

2. Experimental details

2.1. Chemicals and instruments

1,10-Phenanthrolin-5-amine(Phen-NH_2,98.04%) was provided by Shanghai Bide Pharmatech Co., Ltd. 3-Isocyanatopropyltriethoxysilane(ICPTES, 95%)was provided by Shanghai Macklin Biochemical Technology Co., Ltd. $EuCl_3 \cdot 6H_2O$ (99.9%, metals basis), fumed silica (SiO_2, 99%, metals basis), methyl methacrylate (MMA, 99%) and dibenzoyl peroxide (BPO, 75%)was provided by Shanghai Aladdin Biochemical Technology Co., Ltd. 2-Thenoyltrifluoroacetone (TTA, 99%) was provided by JiaXing SiCheng Chemical Co., Ltd. The anhydrous *N*,*N*-dimethylformamide (DMF) and xylene were prepared by distillation after dehydrating the corresponding reagent with magnesium sulfate. Other reagents used in the research, such as ammonia, anhydrous ethanol and petroleum ether, were from Sinopharm Chemical Reagent Co., Ltd.

Fourier Transform Infrared Spectroscopy (FTIR) was characterized by Agilent Cary 630. Fluorescence data were tested with Gangdong F-320 fluorescence spectrophotometer. Ultraviolet-visible (UV-Vis) absorption spectrum were tested with Yoke T-N6000 Plus UV-Vis Spectrophotometer. Thermogravimetric (TG) analysis was performed on a Netzsch STA 449 F3 instrument under a nitrogen atmosphere to ensure inert conditions. Transmission Electron Microscope (TEM) and Energy Dispersive Spectrometer (EDS) were characterized by the Thermo Fisher Talos F200S G2. The scanning electron microscope (SEM) images were captured by a Zeiss Sigma 300.

2.2 Synthesis of complex $[Eu(TTA)_3(H_2O)_2]$

The europium complex $[Eu(TTA)_3(H_2O)_2]$ was synthesized according to the modified literature method.[80] Typically, 3 mmol of TTA was dissolved in 50 mL ethanol and then mixed with a water solution of 1 mmol of $EuCl_3 \cdot 6H_2O$ in a agitated state. Gradually adjust the pH of the mixed solution to 7–8 using ammonia water, and then heat the reaction system to reflux for 0.5 h. While cooling to room temperature, oil-like precipitates form. The precipitates should be collected, rinsed several times with distilled water, and dried under vacuum at 50 °C. Next, the precipitates are washed with petroleum ether to remove any unreacted TTA, followed by a second drying step under vacuum at 50 °C. Lastly, the final product $[Eu(TTA)_3(H_2O)_2]$ was collected.

2.3 Surface modification of fumed silica with Phen-NH_2

The fumed silica was surface modified according to the following procedure. Firstly, 5 mmol of ICPTES and 12 mmol of Phen-NH_2 were dissolved in 30 mL anhydrous DMF. The mixture was transferred to a round-bottomed flask and stirred at 65 °C for 8 hours, followed by vacuum distillation to remove the DMF. Then, 30 mL of a pre-dispersed anhydrous xylene suspension containing 2 g silica spheres was directly added to the reaction flask. The mixture was subsequently stirred and reacted at 115 °C for 8 hours. The surface-modified silica spheres were collected *via* centrifugation. After removing the supernatant, the spheres were re-dispersed in 30 mL anhydrous ethanol and subsequently collected again by centrifugation. This process of centrifugation, re-dispersion in anhydrous ethanol, and re-centrifugation was repeated ten times. Finally, the collected silica spheres were vacuum-dried at 40 °C. The resulting product was designated as SiO_2-Phen.

2.4 Europium complex functionalization of fumed silica

Usually, disperse 500 mg SiO_2 into 10 mL ethanol solution containing 100 mg of $[Eu(TTA)_3(H_2O)_2]$. The mixture was first ultrasonicated for 30 min, followed by stirring at room temperature for 24 h to ensure complete coordination reaction. Europium complex-functionalized silica microspheres were collected *via* a process similar to that used for SiO_2-Phen, specifically "centrifugation–redispersion–recentrifugation". For each re-dispersion step, 10 mL ethanol was employed, and the entire process was repeated 10 times. Finally, the collected products were vacuum-dried at room temperature and designated as SiO_2-Phen-$Eu(TTA)_3$.

2.5 Fabrication of PMMA doped with europium complex modified silica

In a 25 mL round-bottom flask, 9 g MMA, 90 mg SiO_2-Phen-Eu(TTA)$_3$, and 9 mg BPO were added. The mixture was then ultrasonicated for 10 minutes before being transferred to an oil bath at 85 °C for magnetic stirring under a controlled stirring speed of 600 rpm. When the viscosity of the reaction system becomes comparable to that of glycerol, ceased heating and slowly poured the reaction mixture into the mold. Transfer the mold to a pre-heated oven and allow it to harden at 50 °C for 24 h. Subsequently, increase the temperature to 100 °C and maintain it for 1.5 h to ensure the reaction proceeds to completion. Finally, a slightly yellowish product was obtained and designated as SiO_2-Phen-Eu(TTA)$_3$@PMMA.

3. Results and discussion

It is well established that many silica-based materials possess a high density of reactive hydroxyl groups on their surfaces. Extensive research has demonstrated that coupling modification leveraging these surface hydroxyl groups represents an optimal strategy for designing various functionalized silica-based materials. As illustrated in Scheme 1, to impart coordination growth capability to the surface of silica spheres, we first synthesized a chelating silane coupling agent *via* the nucleophilic addition reaction of Phen-NH_2 with ICPTES. Subsequently, this agent was covalently attached to the silica sphere surface through the condensation reaction between the silane oxygen group and the silanol groups, yielding SiO_2-Phen with excellent chelating property. Owing to the superior chelating ability of the Phen groups anchored on the silica surface, they can effectively displace the coordinated water in [Eu(TTA)$_3$(H_2O)$_2$], enabling the loading of [Eu(TTA)$_3$Phen] moieties onto the silica surface. Thus, a silica sphere functionalized with a europium complex, exhibiting exceptional fluorescence luminescence performance, was obtained. To further showcase the application potential of this fluorescent nanomaterial, it was successfully incorporated into a PMMA bulk material *via in situ* polymerization, producing an organic glass material that emits vivid red fluorescence under ultraviolet (365 nm) irradiation (refer to the inset in Scheme 1). Furthermore, the microstructural morphology of the SiO_2-Phen-Eu(TTA)$_3$@PMMA composite was systematically characterized using a scanning electron microscope. As shown in Fig. 1, these SEM images were acquired by scanning the cross-sectional surfaces of the material. From Fig. 1, it can be observed that the composite is composed of polymer particles with sizes ranging from tens to hundreds of nanometers, a structural characteristic typical of PMMA/SiO_2 composite materials.[81] As shown in Fig. 1A–C, SiO_2-Phen-Eu(TTA)$_3$ is uniformly dispersed within the PMMA matrix without any surface agglomeration, and no significant phase separation is observed in the cross-sectional morphology of the material.

Most of the previous studies on the fluorescence modification of silicon-based materials have predominantly focused on laboratory-synthesized silicon-based materials. In this work, we selected fumed silica, which is highly commercialized and amenable to large-scale production, as the carrier material. The particle size distribution of raw fumed silica is approximately 20 to 30 nm. As shown in Fig. 2(1) and (2), the raw fumed silica exhibits significant agglomeration, resulting in an indistinct particle size distribution. After surface modification, the dispersibility of fumed silica is markedly enhanced, allowing for the clear observation of a well-defined silica sphere structure. This improvement in dispersibility can be attributed to the synergistic effects of multiple ultrasonic treatment and the steric hindrance provided by the larger europium complex groups grafted onto the silica surface, which effectively prevent particle agglomeration. During the TEM analysis, EDS measurements were also performed, as illustrated in Fig. S1.† The EDS results confirmed the presence of a low concentration of Eu elements in the system, while the corresponding HAADF (high angle annular dark field) image revealed the uniform distribution of Eu elements within the material. These findings collectively provide compelling evidence for the successful loading of europium complexes onto the surface of fumed silica. These results collectively provide an evidence for the successful loading of europium complexes onto the surface of fumed silica.

It is widely recognized that FTIR is a standard analytical technique for characterizing the composition of materials and molecular structures. To further examine the surface modification of silica materials, FTIR spectra were obtained for raw fumed silica (SiO_2), Phen-NH_2 modified fumed silica (SiO_2-Phen), and europium complexes modified fumed silica (SiO_2-Phen-Eu(TTA)$_3$). Fig. 3(1) presents the FTIR spectrum of the classic silica material.[82] The strong and broad absorption band at 1103 cm^{-1} corresponds to the antisymmetric stretching vibration (ν_{as}) of Si–O–Si bonds, while the peak at 805 cm^{-1} is attributed to the symmetric stretching vibration (ν_s) of Si–O–Si bonds. The broad peak at 3421 cm^{-1} is associated with the stretching vibration (ν) of O–H in the adsorbed water molecules, and the peak near 1633 cm^{-1} corresponds to the bending vibration (δ) of H–O–H in water. The peak at 969 cm^{-1} is assigned to the stretching vibration absorption (ν) of Si–OH groups. Compared to Fig. 3(1), the FTIR spectrum of SiO_2-Phen (Fig. 3(2)) exhibits an additional prominent absorption peak at 1551 cm^{-1}, corresponding to the stretching vibration (ν) of the C=N double bond in the aromatic heterocyclic ring of the Phen-NH_2. Furthermore, multiple absorption peaks observed between 3100 cm^{-1} and 2800 cm^{-1} can be attributed to various C–H bonds present in aromatic rings, methylene groups, and residual methyl groups. These newly emerged absorption peaks provide strong evidence that Phen-NH_2 has been successfully grafted onto the fumed silica surface. The spectrum of SiO_2-Phen-Eu(TTA)$_3$ presents a very strong absorption at 1610 cm^{-1}, which can be ascribed to the stretching vibration absorption (ν) of C=O on the chelating ring formed between Eu(III) and TTA. This absorption peak combines with the bending vibration of H–O–H in water to form a strong and broad absorption peak. Meanwhile, the two absorption peaks at 1416 cm^{-1} and 1357 cm^{-1} in the spectrum of SiO_2-Phen-Eu(TTA)$_3$ should be ascribed to the stretching vibrations (ν_s) of C=C, C=S in the

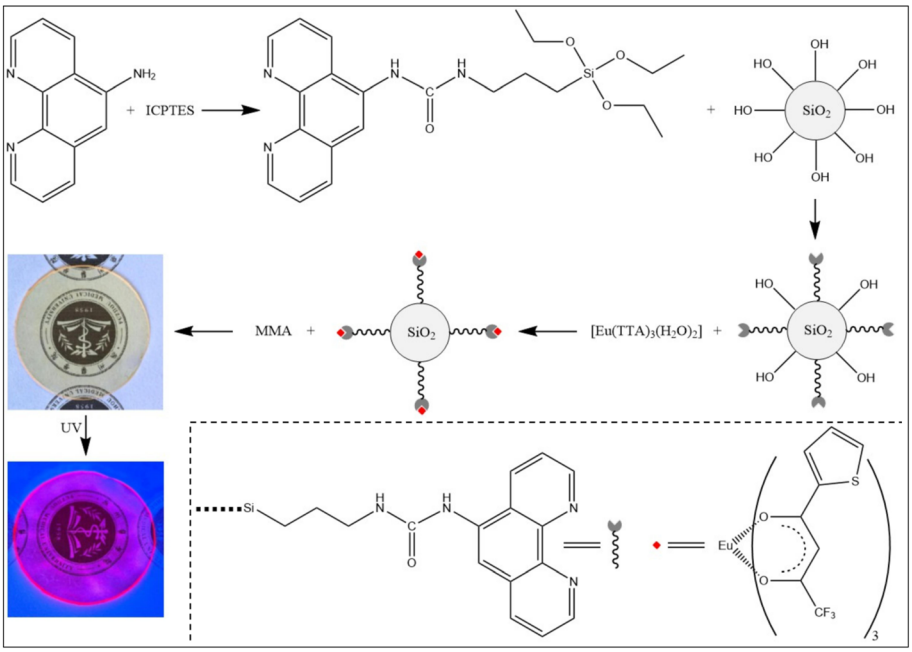

Scheme 1 The preparation route, photos and the photos under ultraviolet light (365 nm) irradiation of SiO_2-Phen-Eu(TTA)$_3$@PMMA.

thienyl heterocycle.[83] In addition, the –CF_3 group in the TTA moiety exhibits a strong absorption peak at approximately 1180 cm^{-1}. However, this peak overlaps with the highly intense ν_{as}(Si–O–Si) band, resulting in a shoulder peak. This overlap also accounts for the distinct appearance of the ν_{as}(Si–O–Si) band in SiO_2-Phen-Eu(TTA)$_3$ compared to other spectra.[84] In contrast to the spectrum of SiO_2-Phen, these newly emerged absorption peaks can be construed as compelling evidence for the attachment of europium complexes on the surface of fumed silica.

To further validate the loading status of europium complexes on the surface of fumed silica, the thermogravimetric (TG)

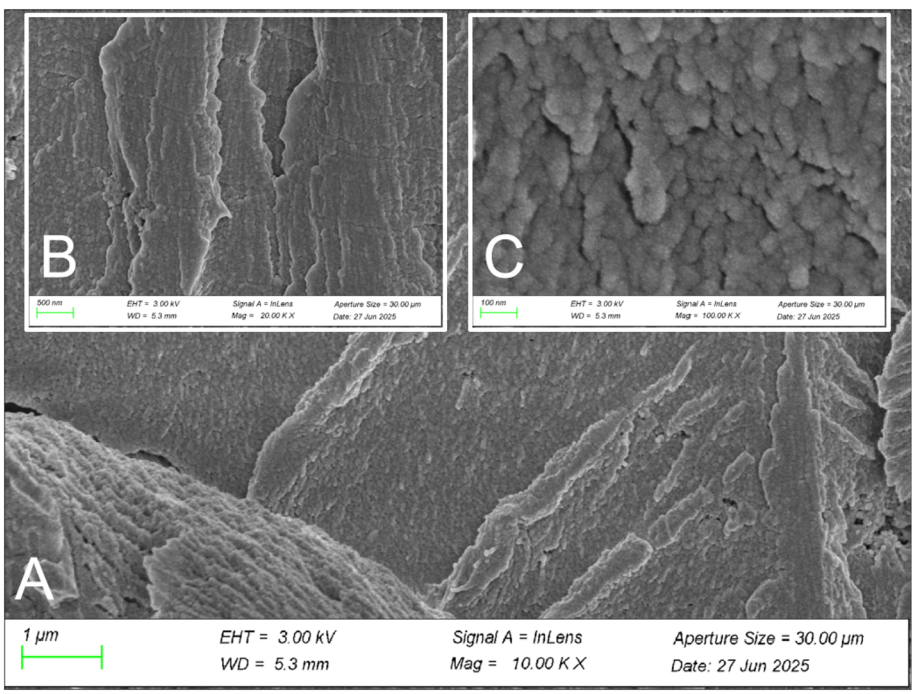

Fig. 1 SEM images of the SiO_2-Phen-Eu(TTA)$_3$@PMMA. The lengths of the rulers in the figure are 1 μM (A), 500 nm (B) and 100 nm (C), respectively.

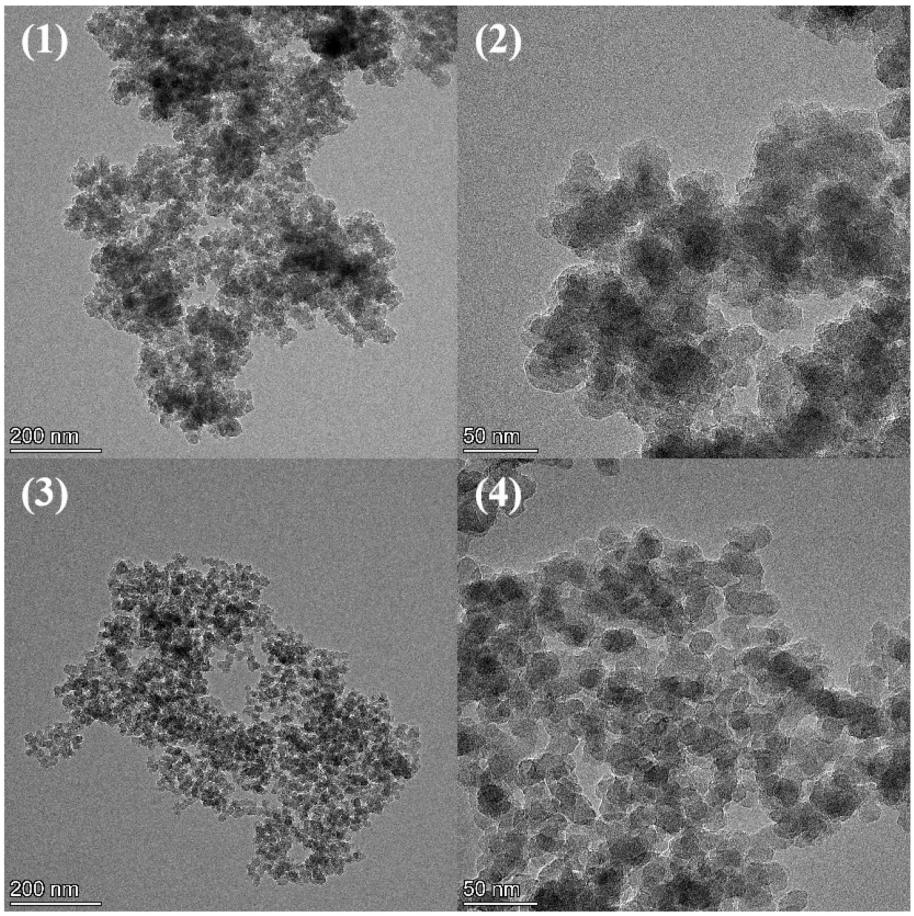

Fig. 2 (1) & (2) TEM of raw fumed silica; (3) & (4) TEM of SiO_2-Phen-Eu(TTA)$_3$.

analysis of the SiO_2-Phen-Eu(TTA)$_3$ was conducted under an N_2 atmosphere, with a heating rate of 20 °C min^{-1} from room temperature to 1000 °C. As illustrated in the Fig. 4(1), the thermal decomposition process of sample can be divided into four distinct stages as the temperature increases. The first stage, ranging from room temperature to about 190 °C, corresponds to

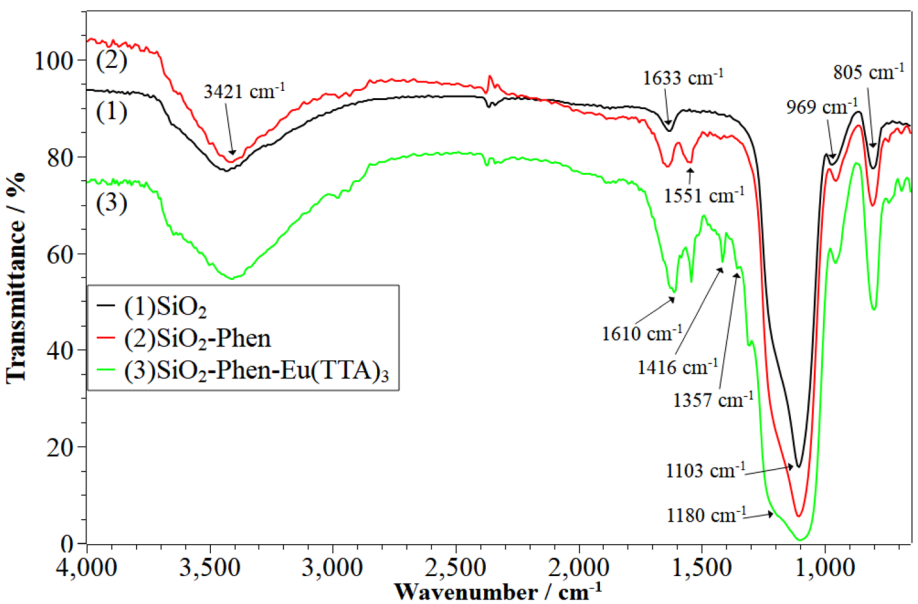

Fig. 3 FTIR images of SiO_2, SiO_2-Phen and SiO_2-Phen-Eu(TTA)$_3$.

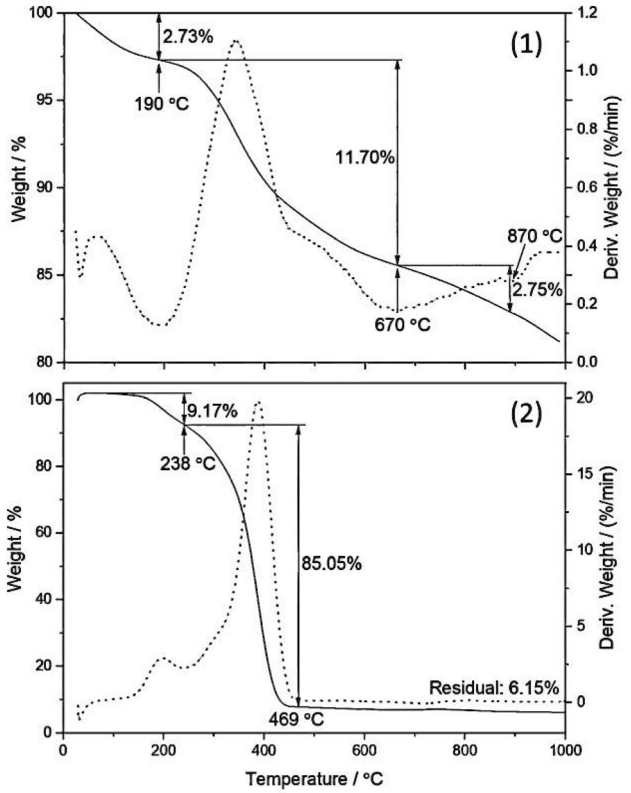

Fig. 4 TG analysis curve of SiO_2-Phen-Eu(TTA)$_3$ (1) and SiO_2-Phen-Eu(TTA)$_3$@PMMA (2).

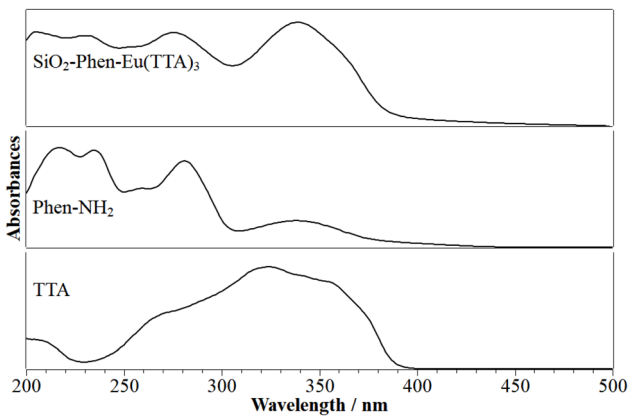

Fig. 5 UV-Vis absorption spectra of the TTA, Phen and SiO_2-Phen-Eu(TTA)$_3$.

the desorption of physically adsorbed water and partial removal of bound water, resulting in a weight loss of approximately 2.73%. The second stage, occurring between 190 °C and 670 °C, represents the primary decomposition phase, which is attributed to the breakdown and volatilization of the europium complexes[85] and silane coupling agents anchored on the SiO_2 surface, leading to a weight loss of about 11.7%. The third and fourth stages correspond to the further decomposition of residual organic materials on the SiO_2 surface and the dehydroxylation of surface hydroxyl groups at elevated temperatures, respectively. In conjunction with additional characterizations, it is evident that the 11.7% weight loss observed in the second stage indeed includes contributions from the europium complexes, providing robust evidence for their successful loading onto the fumed silica surface. Under the same conditions, the TG analysis curve of SiO_2-Phen-Eu(TTA)$_3$@PMMA was also obtained. As illustrated in Fig. 4(2), the thermal decomposition process of the sample can be clearly divided into two distinct stages. The first stage, occurring before 238 °C, results in a weight loss of approximately 9.17%, which is likely attributed to the evaporation of residual methyl methacrylate MMA and its oligomer. The second stage spans from 238 °C to approximately 469 °C, during which a significant mass reduction of about 85.05% occurs. This mass loss corresponds to the typical decomposition behavior observed in PMMA nanocomposites,[86] primarily attributed to the thermal degradation of the PMMA matrix, with a minor contribution arising from the decomposition of rare earth complexes supported on the silica nanoparticles. Finally, approximately 6.15% of the original mass remains, which is likely composed of inorganic residues such as SiO_2 and Eu-containing compounds. Notably, this residual mass exceeds the initially added particle content, suggesting considerable material loss during the polymerization of MMA and the composite formation process.

The fluorescence emission properties of rare earth down-conversion luminescent materials are closely associated with their UV-Vis absorption spectra. To this end, the UV-Vis absorption characteristics of the TTA, Phen-NH_2, and the SiO_2-Phen-Eu(TTA)$_3$ were characterized. As depicted in Fig. 5, TTA exhibits a broad and intense absorption band spanning 240–400 nm, whereas Phen-NH_2 demonstrates stronger absorption within the 200–300 nm range. Obviously, the spectra of SiO_2-Phen-Eu(TTA)$_3$ effectively integrates the absorption ranges of TTA and Phen-NH_2, resulting in a strong absorption coefficient across the entire UV region. This is primarily attributed to the large conjugated structures of both β-diketone molecules (TTA) and the second ligand (Phen-NH_2), as well as the complementary nature of their UV absorption ranges. Consequently, SiO_2-Phen-Eu(TTA)$_3$ efficiently absorbs UV light energy, which serves as a critical foundation for its ability to emit intense fluorescence under UV excitation.

The fluorescence excitation spectra of europium complex-functionalized fumed silica and its corresponding PMMA-doped composite had been shown in Fig. 6(1) and (3). As illustrated in the figure, the fluorescence excitation spectra of SiO_2-Phen-Eu(TTA)$_3$ and SiO_2-Phen-Eu(TTA)$_3$@PMMA exhibit high similarity. Both materials exhibit a broad and intense excitation band in the range of 280–420 nm, which is in agreement with the findings from the ultraviolet absorption analysis. Although there are minor differences in their maximum excitation wavelengths, these peaks are predominantly centered around 370 nm. For the purpose of facilitating comparison, the fluorescence emission spectra of SiO_2-Phen-Eu(TTA)$_3$ and SiO_2-Phen-Eu(TTA)$_3$@PMMA were measured under an excitation wavelength of 373 nm. As depicted in

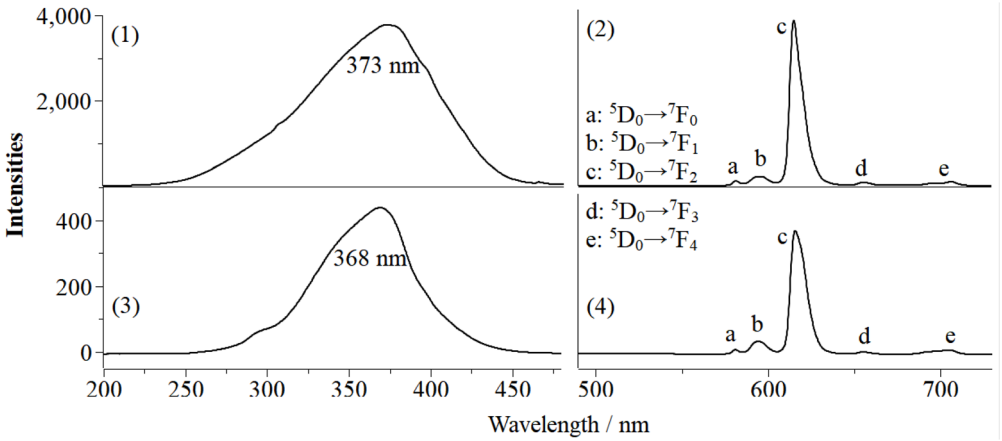

Fig. 6 Fluorescence excitation and emission spectra of SiO_2-Phen-Eu(TTA)$_3$ (1 and 2) and SiO_2-Phen-Eu(TTA)$_3$@PMMA (3 and 4).

Fig. 6(2) and (4), both materials display the characteristic fluorescence emission features of rare earth europium complexes. As shown in figure, five distinct emission bands can be clearly observed, with the positions of the emission peaks being highly consistent. From left to right, these peaks are located at approximately 581 nm, 595 nm, 615 nm, 656 nm, and 707 nm, corresponding to the $^5D_0 \rightarrow {}^7F_0$, $^5D_0 \rightarrow {}^7F_1$, $^5D_0 \rightarrow {}^7F_2$, $^5D_0 \rightarrow {}^7F_3$ and $^5D_0 \rightarrow {}^7F_4$ transitions of Eu^{3+} ions, respectively. Among these, the $^5D_0 \rightarrow {}^7F_2$ emission peak at 615 nm exhibits significantly higher intensity compared to the others and is characteristic of narrow-band emission. Given that the $^5D_0 \rightarrow {}^7F_2$ transition represents a strong electric dipole transition, whereas the $^5D_0 \rightarrow {}^7F_1$ transition corresponds to a weak magnetic dipole transition, the intensity ratio I ($^5D_0 \rightarrow {}^7F_2$)/$I$ ($^5D_0 \rightarrow {}^7F_1$) is frequently employed as an indicator of the symmetry of the chemical environment surrounding Eu^{3+} ions. The I ($^5D_0 \rightarrow {}^7F_2$)/$I$ ($^5D_0 \rightarrow {}^7F_1$) intensity ratios for SiO_2-Phen-Eu(TTA)$_3$ and SiO_2-Phen-Eu(TTA)$_3$@PMMA were calculated to be 14.3 and 10.1, respectively. Although this value decreased upon doping the europium complex-functionalized fumed silica into the PMMA matrix, it remained at a relatively high level. This suggests that the Eu^{3+} ions were in a coordination environment with relatively low symmetry both before and after doping. Therefore, under the excitation of 365 nm light, the final product SiO_2-Phen-Eu(TTA)$_3$@PMMA exhibits a vivid red color. Furthermore, under identical testing conditions, the fluorescence intensity of SiO_2-Phen-Eu(TTA)$_3$@PMMA is approximately one-tenth of that of the undoped SiO_2-Phen-Eu(TTA)$_3$. Despite this significant reduction, given that the doping level of SiO_2-Phen-Eu(TTA)$_3$@PMMA is relatively low, this result still supports the conclusion that the europium complex-functionalized fumed silica reported here exhibits superior fluorescence emission performance.

It is well established that rare earth complex luminescent materials typically exhibit relatively long fluorescence lifetimes. To further explore the photophysical properties of europium complex-functionalized fumed silica both before and after doping, we had measured their fluorescence intensity decay curves. As shown in Fig. 7, both of the materials displayed a double-exponential decay behavior, the average fluorescence lifetimes of the SiO_2-Phen-Eu(TTA)$_3$ and SiO_2-Phen-Eu(TTA)$_3$@PMMA were calculated to be 166 ms and 65 ms, respectively. Owing to its relatively low doping concentration, SiO_2-Phen-Eu(TTA)$_3$@PMMA exhibited weaker fluorescence

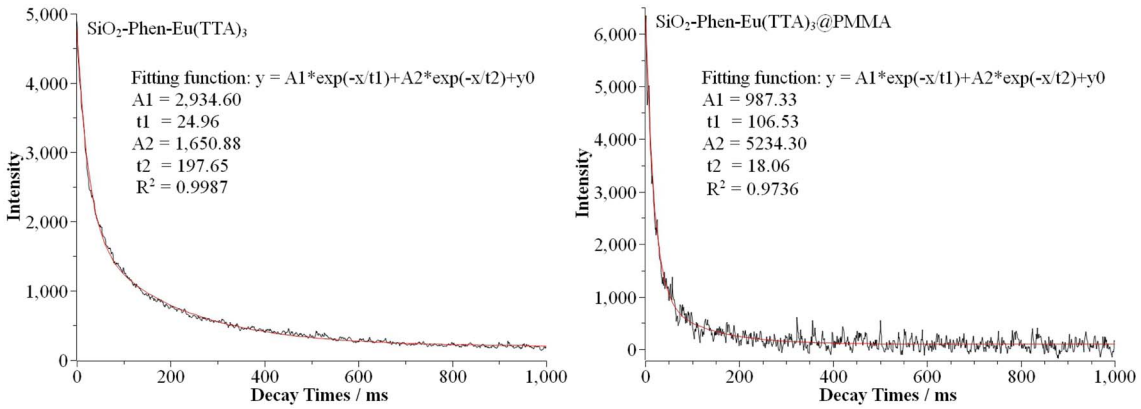

Fig. 7 Fitting results of the fluorescence lifetime of SiO_2-Phen-Eu(TTA)$_3$ and SiO_2-Phen-Eu(TTA)$_3$@PMMA.

intensity, which resulted in a lower fitting accuracy and a shorter fluorescence lifetime.

4. Conclusions

A novel lanthanide organic–inorganic hybrid fluorescent materials with excellent luminescent properties were successfully synthesized using commercialized silica materials as the matrix. Subsequently, the europium-modified fumed silica was doped into PMMA to fabricate a monolithic fluorescent organic glass. Additionally, FTIR, UV-Vis, TEM, TG, and fluorescence characterizations were employed to thoroughly investigate the synthesis process and photophysical properties of the resulted material. The results indicate that the europium complex has been successfully grafted onto the surface of fumed silica. The resultant hybrid material exhibits strong characteristic fluorescence of Eu^{3+} ions even at a low loading level of the europium complex. Furthermore, after doping into PMMA at the relatively low concentration, the obtained organic glass maintains excellent fluorescence emission performance, with the entire piece glowing red under 365 nm lights. In summary, the approach presented here is an efficient and cost-effective method for preparing rare earth hybrid luminescent materials, which holds significant reference value for researchers dedicated to developing novel rare earth hybrid luminescent materials.

Data availability

The data supporting this article have been included as part of the ESI.†

Conflicts of interest

The authors declare that they have no known competing financial interests or personal relationships that could have appeared to influence the work reported in this paper.

Acknowledgements

This work was supported by the Science and Technology Research Project of Jiangxi Provincial Department of Education (GJJ218108).

References

1 Ravina, K. Poria, M. K. Sahu, A. Kumar, Anu, S. Dahiya, N. Deopa and A. S. Rao, *RSC Adv.*, 2023, **13**, 33675–33687.
2 S. Vaidyanathan, *J. Mater. Chem. C*, 2023, **11**, 8649–8687.
3 M. K. Hossain, S. Hossain, M. H. Ahmed, M. I. Khan, N. Haque and G. A. Raihan, *ACS Appl. Electron. Mater.*, 2021, **3**, 3715–3746.
4 D. Valiev, S. Stepanov, O. Khasanov, E. Dvilis, E. Polisadova and V. Paygin, *Opt. Mater.*, 2019, **91**, 396–400.
5 K. Binnemans, *Chem. Rev.*, 2009, **109**, 4283–4374.
6 Q. L. Gao, H. Y. Wang, C. X. Liu, L. H. Luo, X. Li, Q. Jiang, Y. Ji, T. T. Zheng and C. Xia, *Chin. J. Chem.*, 2025, **43**, 205–218.
7 Y. Zhang, S. Liu, Z. S. Zhao, Z. F. Wang, R. Y. Zhang, L. Liu and Z. B. Han, *Inorg. Chem. Front.*, 2021, **8**, 590–619.
8 Y. K. Yuan, G. Xue, S. F. Wang and X. L. Zhang, *Appl. Mech. Mater.*, 2013, **320**, 413–418.
9 Y. H. Xu, X. Yang, Y. T. Li, Y. Zhao, X. Shu, G. Y. Zhang, T. N. Yang, Y. T. Liu, P. K. Wu and Z. Ding, *Nanomaterials*, 2024, 14.
10 W. F. Qiao, W. Q. Liu, D. M. Yin, N. Ding, S. L. Zhao, H. X. Xiu, C. Liu, Y. Wang, M. He, C. L. Wang, L. M. Wang and Y. Cheng, *Chem. Eng. J.*, 2024, **495**, 153489.
11 C. E. Lundin, *J. Phys. Colloques*, 1979, **40**, 286–291.
12 S. Erdmann, T. Klüner and H. İ. Sözen, *J. Magn. Magn. Mater.*, 2023, **572**, 170645.
13 L. Bessais, *Materials*, 2022, **15**, 201.
14 K. Strnat, The recent development of permanent magnet materials containing rare earth metals, *IEEE Trans. Magn.*, 1970, **6**(2), 182–190.
15 W. Leal Filho, R. Kotter, P. G. Özuyar, I. R. Abubakar, J. H. Eustachio and N. R. Matandirotya, *Sustainability*, 2023, **15**, 1919.
16 C. Z. Wang, in *Theory and Application of Rare Earth Materials*, ed. Wang, C., Springer Nature Singapore, Singapore, 2023, pp. 271–291.
17 C. Y. Lv, X. Q. Wang, Q. Zhang and Y. J. Zhang, *Mater. Chem. Front.*, 2023, **7**, 2809–2827.
18 L. P. Li, T. Y. Li, Y. Hu, C. Y. Cai, Y. Q. Li, X. F. Zhang, B. L. Liang, Y. M. Yang and J. R. Qiu, *Light:Sci. Appl.*, 2022, **11**, 51.
19 S. B. Li, L. Zhou and H. J. Zhang, *Light:Sci. Appl.*, 2022, **11**, 177.
20 M. Hasegawa, H. Ohmagari, H. Tanaka and K. Machida, *J. Photochem. Photobiol., C*, 2022, **50**, 100484.
21 J. G. Bünzli, in *Handbook on the Physics and Chemistry of Rare Earths*, ed. Bünzli, J. G. and Pecharsky, V. K., Elsevier, 2016, vol. 50, pp. 141–176.
22 I. Gupta, S. Singh, S. Bhagwan and D. Singh, *Ceram. Int.*, 2021, **47**, 19282–19303.
23 X. Song, M. Chang and M. Pecht, *JOM*, 2013, **65**, 1276–1282.
24 A. de Bettencourt-Dias, *Dalton Trans.*, 2007, 2229–2241.
25 P. C. D. Sousa Filho, J. F. Lima, O. A. Serra, P. C. D. Sousa Filho, J. F. Lima and O. A. Serra, *N. Engl. J. Med.*, 1973, **288**, 914–915.
26 J. X. Pan, J. Z. Lu, Y. C. Shang, Y. Li and B. Yan, *J. Mater. Chem. C*, 2025, **13**, 1198–1206.
27 S. N. Zhao, G. B. Wang, D. Poelman and P. V. Voort, *Materials*, 2018, **11**, 572.
28 F. Faridbod, M. R. Ganjali and M. Hosseini, in *Lanthanide-Based Multifunctional Materials*, ed. Martín-Ramos, P. and Ramos Silva, M., Elsevier, 2018, pp. 411–454.
29 B. Yan, *Inorg. Chem. Front.*, 2021, **8**, 201–233.
30 W. Mnasri, M. Parvizian and S. Ammar-Merah, *Nanomaterials*, 2021, **11**(2), 354.
31 Y. W. Zhang and G. Han, *Lanthanide-doped Upconverting Nanoparticles for Biological Applications*, Imperial College Press, 2015, pp. 37–64.
32 L. Prodi, E. Rampazzo, F. Rastrelli, A. Speghini and N. Zaccheroni, *Chem. Soc. Rev.*, 2015, **44**, 4922–4952.

33 P. Kumar, S. Singh and B. K. Gupta, *Nanoscale*, 2016, **8**, 14297–14340.
34 M. Gao, J. F. Li, X. Y. Lu, R. K. Li, C. L. Hong, S. C. Zhao and G. M. Li, *Inorg. Chim. Acta*, 2024, **560**, 121813.
35 Y. L. Liu, K. L. Ai and L. H. Lu, *Nanoscale*, 2011, **3**, 4804–4810.
36 Y. Lin, M. Karlsson and M. Bettinelli, in *Photoluminescent Materials and Electroluminescent Devices*, ed Armaroli, N. and Bolink, H. J., Springer International Publishing, Cham, 2017, pp. 309–355.
37 C. Feldmann, T. Jüstel, C. R. Ronda and P. J. Schmidt, *Adv. Funct. Mater.*, 2003, **13**, 511–516.
38 H. A. Höppe, *Angew. Chem., Int. Ed.*, 2009, **48**, 3572–3582.
39 R. Janicki, A. Mondry and P. Starynowicz, *Coord. Chem. Rev.*, 2017, **340**, 98–133.
40 Q. T. Chen, J. Zhang, Q. F. Ye, S. Q. Qin, L. Y. Li, M. Y. Teng and W. Y. Wong, *Molecules*, 2025, **30**, 1342.
41 X. X. Wang, Y. F. Hao, J. Du, Y. Y. Ma, J. J. Zhao, N. Ren and J. J. Zhang, *J. Saudi Chem. Soc.*, 2023, **27**, 101763.
42 B. Yan, H. Zhang, S. Wang and J. Ni, *J. Photochem. Photobiol., A*, 1998, **116**, 209–214.
43 Q. P. Li, Q. Q. Wen, Z. A. Fang, Y. D. Wang, H. X. Ouyang, Q. Wang and M. Wei, *RSC Adv.*, 2024, **14**, 30037–30044.
44 K. Nehra, A. Dalal, A. Hooda, S. Bhagwan, R. K. Saini, B. Mari, S. Kumar and D. Singh, *J. Mol. Struct.*, 2022, **1249**, 131531.
45 G. G. Condorelli, G. Malandrino and I. L. Fragalà, *Coord. Chem. Rev.*, 2007, **251**, 1931–1950.
46 D. F. Wu, Z. Liu, P. Ren, X. H. Liu, N. Wang, J. Z. Cui and H. L. Gao, *Dalton Trans.*, 2019, **48**, 1392–1403.
47 K. Binnemans, in *Handbook on the Physics and Chemistry of Rare Earths*, ed. Gschneidner, K. A., Bünzli, J. G. and Pecharsky, V. K., Elsevier, 2005, vol. 35, pp. 107–272.
48 N. Sabbatini, M. Guardigli and I. Manet, in *Handbook on the Physics and Chemistry of Rare Earths*, Elsevier, 1996, vol. 23, pp. 69–119.
49 P. A. Tanner, W. Thor, Y. H. Zhang and K. L. Wong, *J. Phys. Chem. A*, 2022, **126**, 7418–7431.
50 E. G. Moore, A. P. S. Samuel and K. N. Raymond, *Acc. Chem. Res.*, 2009, **42**, 542–552.
51 X. Y. Zhao, J. Wang, Q. S. Yang, D. L. Fu and D. K. Jiang, *Anal. Methods*, 2021, **13**, 3994–4000.
52 D. K. Dinga, M. Bredol and U. Kynast, *J. Phys. Chem. A*, 2023, **127**, 1130–1140.
53 P. Li and H. R. Li, *Coord. Chem. Rev.*, 2021, **441**, 213988.
54 A. K. Singh, *Coord. Chem. Rev.*, 2022, **455**, 214365.
55 J. Hayashi, S. Shoji, Y. Kitagawa and Y. Hasegawa, *Coord. Chem. Rev.*, 2022, **467**, 214607.
56 B. Yan, *RSC Adv.*, 2012, **2**, 9304–9324.
57 J. Feng and H. J. Zhang, *Chem. Soc. Rev.*, 2013, **42**, 387–410.
58 L. D. Carlos, R. A. S. Ferreira, V. D. Z. Bermudez and S. J. L. Ribeiro, *Adv. Mater.*, 2009, **21**, 509–534.
59 Q. Li and B. Yan, *J. Rare Earths*, 2019, **37**, 113–123.
60 B. Yan, *Chem.–Eur. J.*, 2023, **29**, e202301108.
61 G. Zhang, L. F. Mei, J. J. Ding, K. Su, Q. F. Guo, G. C. Lv and L. B. Liao, *J. Rare Earths*, 2022, **40**, 1360–1370.
62 H. R. Li, J. Lin, H. J. Zhang, L. S. Fu, Q. G. Meng and S. B. Wang, *Chem. Mat.*, 2002, **14**, 3651–3655.
63 A. M. G. Mutti, F. S. M. Canisares, J. A. O. Santos, B. C. Santos, D. G. S. M. Cavalcante, A. E. Job, A. M. Pires and S. A. M. Lima, *J. Sol-Gel Sci. Technol.*, 2023, **107**, 754–770.
64 K. S. Ambili and J. Thomas, *J. Porous Mater.*, 2020, **27**, 755–764.
65 D. C. Yao, S. F. Wang, P. Li and H. R. Li, *J. Lumin.*, 2019, **215**, 116641.
66 H. R. Li and P. Li, *Chem. Commun.*, 2018, **54**, 13884–13893.
67 Y. G. Wang, P. Li, S. F. Wang and H. R. Li, *J. Rare Earths*, 2019, **37**, 451–467.
68 D. T. de Araujo, K. J. Ciuffi, E. J. Nassar, M. A. Vicente, R. Trujillano, P. S. Calefi, V. Rives and E. H. de Faria, *J. Phys. Chem. C*, 2017, **121**, 5081–5088.
69 J. H. Ma, D. Q. Yang, X. F. Song and Y. G. Wang, *J. Lumin.*, 2019, **212**, 126–132.
70 M. Y. Wang, G. Huang, J. H. Yu and Q. P. Li, *Optoelectron. Adv. Mater.-Rapid Commun.*, 2018, **12**, 547–552.
71 M. Gil-Kowalczyk, R. Łyszczek, A. Jusza and R. Piramidowicz, *Materials*, 2021, **14**, 3156.
72 O. Kotova, S. J. Bradberry, A. J. Savyasachi and T. Gunnlaugsson, *Dalton Trans.*, 2018, **47**, 16377–16387.
73 B. S. D. Onishi, B. H. Costa, L. Marchiori, B. D. de Freitas, R. S. Pugina, J. R. Bartlett, L. D. Carlos, E. P. Ferreira-Neto and S. J. L. Ribeiro, *J. Sol-Gel Sci. Technol.*, 2025, **113**, 86–108.
74 L. Trupp, M. C. Marchi and B. C. Barja, *J. Sol-Gel Sci. Technol.*, 2022, **102**, 63–85.
75 R. Ciriminna, A. Fidalgo, V. Pandarus, F. Béland, L. M. Ilharco and M. Pagliaro, *Chem. Rev.*, 2013, **113**, 6592–6620.
76 N. Tan, Y. Ning, P. Hu, Y. Feng, Q. Li, C. Lin, Z. Cao, Y. Zhang and J. Zeng, *J. Therm. Anal. Calorim.*, 2022, **147**, 7077–7097.
77 B. Sun, G. Zhou and H. Zhang, *Prog. Solid State Chem.*, 2016, **44**, 1–19.
78 Q. P. Li and Y. Zhou, *Molecules*, 2023, **28**, 2013.
79 F. Hoffmann, M. Cornelius, J. Morell and M. Fröba, *Angew. Chem., Int. Ed.*, 2006, **45**, 3216–3251.
80 I. Olszowska-Łoś, T. Ratajczyk, I. S. Pieta, A. Siejca, J. Niedziółka-Jönsson and A. Leśniewski, *Anal. Chem.*, 2020, **92**, 15671–15678.
81 G. Soni, S. Srivastava, P. Soni, P. Kalotra and Y. K. Vijay, *Mater. Res. Express*, 2018, **5**, 15302.
82 C. Carteret, *Spectrochim. Acta, Part A*, 2006, **64**, 670–680.
83 A. P. Duarte, M. Gressier, M. Menu, J. Dexpert-Ghys, J. M. A. Caiut and S. J. L. Ribeiro, *J. Phys. Chem. C*, 2012, **116**, 505–515.
84 J. J. Senkevich, B. W. Woods, B. P. Carrow, R. D. Geil and B. R. Rogers, *Chem. Vap. Deposition*, 2006, **12**, 285–289.
85 A. Ugale, N. T. Kalyani and S. J. Dhoble, *Mater. Sci. Energy Technol.*, 2019, **2**, 57–66.
86 V. Parthasarathy, R. S. Nakandhrakumar, S. Mahalakshmi, P. Senthil Kumar and B. Sundaresan, *J. Inorg. Organomet. Polym. Mater.*, 2020, **30**, 2998–3013.